AGU PUBLICATIONS

JGR

Journal of Geophysical Research: Space Physics

RESEARCH ARTICLE

10.1002/2013JA019490

Key Points:
- The largest equatorial vertical $E \times B$ changes are in longitudinal wave number 1
- The wave number 1 $E \times B$ changes are caused primarily by the SW1 tide and PW1
- The $E \times B$ longitudinal wave number 4 shows no temporal correlation with the SSW

Correspondence to:
A. Maute,
maute@ucar.edu

Citation:
Maute, A., M. E. Hagan, A. D. Richmond and R. G. Roble (2014), TIME-GCM study of the ionospheric equatorial vertical drift changes during the 2006 stratospheric sudden warming, *J. Geophys. Res. Space Physics*, *119*, 1287–1305, doi:10.1002/2013JA019490.

Received 27 SEP 2013
Accepted 21 JAN 2014
Accepted article online 24 JAN 2014
Published online 18 FEB 2014

TIME-GCM study of the ionospheric equatorial vertical drift changes during the 2006 stratospheric sudden warming

A. Maute[1], M. E. Hagan[1], A. D. Richmond[1], and R. G. Roble[1]

[1]High Altitude Observatory, National Center for Atmospheric Research, Boulder, Colorado, USA

Abstract This modeling study quantifies the daytime low-latitude vertical $E \times B$ drift changes in the longitudinal wave number 1 (wn1) to wn4 during the major extended January 2006 stratospheric sudden warming (SSW) period as simulated by the National Center for Atmospheric Research thermosphere-ionosphere-mesosphere electrodynamics general circulation model (TIME-GCM), and attributes the drift changes to specific tides and planetary waves (PWs). The largest drift amplitude change (approximately 5 m/s) is seen in wn1 with a strong temporal correlation to the SSW. The wn1 drift is primarily caused by the semidiurnal westward propagating tide with zonal wave number 1 (SW1), and secondarily by a stationary planetary wave with zonal wave number 1 (PW1). SW1 is generated by the nonlinear interaction of PW1 and the migrating semidiurnal tide (SW2) at high latitude around 90–100 km. The simulations suggest that the *E* region PW1 around 100–130 km at the different latitudes has different origins: at high latitudes, the PW1 is related to the original stratospheric PW1; at midlatitudes, the model indicates PW1 is due to the nonlinear interaction of SW1 and SW2 around 95–105 km; and at low latitudes, the PW1 might be caused by the nonlinear interaction between DE2 and DE3. The time evolution of the simulated wn4 in the vertical $E \times B$ drift amplitude shows no temporal correlation with the SSW. The wn4 in the low-latitude vertical drift is attributed to the diurnal eastward propagating tide with zonal wave number 3 (DE3), and the contributions from SE2, TE1, and PW4 are negligible.

1. Introduction

In the last several years stratospheric sudden warmings (SSWs) have gotten special attention from the ionospheric community. The Sun was extremely quiet during the last extended solar minimum period and more ionospheric observations were available, which made it possible to discover and quantify effects of strong meteorological disturbances such as SSW on the ionosphere. The variation of solar radiation and geomagnetic forcing could not explain the magnitude of the day-to-day ionospheric variability, and the variability of the lower atmosphere was proposed to be another source of ionospheric variability, e.g., *Rishbeth* [2006].

SSWs are one of the most dramatic events in the winter middle atmosphere. They are caused by large planetary waves originating in the troposphere and propagating into the stratosphere. There, they interact with the eastward mean flow, causing a deceleration or reversal of the polar stratospheric winter jet. The weakening of the polar winter jet leads to downward winds in the stratosphere, and therefore adiabatic heating, while in the mesosphere the upward winds cause adiabatic cooling [*Matsuno*, 1971]. These changes to the background atmosphere modulate atmospheric tides that propagate into the middle and upper atmosphere.

During the prolonged stratospheric warming in 2006 a very disturbed vertical temperature structure was observed [e.g., *Manney et al.*, 2008; *Smith et al.*, 2009; *Siskind et al.*, 2010]. The stratopause reformed much higher up, around 80 km, with a temperature increase of up to 70 K at these heights, while there was a strong cooling at the normal stratopause height (i.e., approximately 50 km). The 2006 major SSW was associated with a very large amplitude stationary planetary wave with zonal wave number 1 (PW1) in the stratosphere [*Manney et al.*, 2008].

Goncharenko and Zhang [2008] linked the ion temperature signals to the disturbed stratosphere during the January 2008 SSW event. For the same event, the prenoon vertical $E \times B$ plasma drift increases at Jicamarca correlated well with the enhanced total electron content (TEC) in the equatorial ionization anomaly (EIA) region, suggesting an electrodynamic coupling between the lower atmosphere and the *F* region [*Chau et al.*,2009]. At low latitudes a 50%–150% increase in prenoon total electron content (TEC), and

an approximately 50% decrease in the afternoon TEC in the EIA region, was observed during the 2009 SSW period [*Goncharenko et al.*, 2010a]. Numerous studies focused on the SSW signals in the ionospheric observations [e.g., *Goncharenko et al.*, 2010b; *Pedatella and Forbes*, 2010; *Yue et al.*, 2010; *Pancheva et al.*, 2012; *Lin et al.*, 2013], in the low-latitude vertical drifts [e.g., *Chau et al.*, 2010; *Anderson and Araujo-Pradere*, 2010; *Rodrigues et al.*, 2011], and in the equatorial electrojet [e.g., *Sridharan et al.*, 2009; *Sripathi and Bhattacharyya*, 2012; *Park et al.*, 2012]. In parallel, numerical modeling studies reproduced the observations and were used to examine possible underlying mechanisms [e.g., *Fuller-Rowell et al.*, 2010; *Fang et al.*, 2012; *Jin et al.*, 2012; *Wang et al.*, 2011; *Liu et al.*, 2013a; *Pedatella and Liu*, 2013]. For a more complete review of the effects of SSW events on the ionosphere we refer to *Chau et al.* [2012, and references therein].

Several studies have examined the tidal changes in the *E* region neutral atmosphere during SSW periods [e.g., *Fuller-Rowell et al.*, 2010; *Wang et al.*, 2011; *Fang et al.*, 2012; *Jin et al.*, 2012; *Liu et al.*, 2013b]. *Fang et al.* [2012] examined the effect of migrating tidal components on the low latitude vertical $E \times B$ drift using the Whole Atmosphere Model (WAM) and the Coupled Thermosphere-Ionosphere-Plasmasphere electrodynamics model, showing that the migrating components are responsible for the shift of the daytime upward vertical drift peak to earlier local times, but without attributing it to a specific tidal component. The ionospheric effects of SSW were decomposed into both migrating and nonmigrating tidal harmonics by *Pedatella and Forbes* [2010], *Pancheva et al.* [2012], *Lin et al.* [2013], and others to examine a possible connection with the thermospheric tidal changes. At least two mechanisms can be responsible for the atmosphere-ionosphere coupling [e.g., *Chau et al.*, 2012; *England*, 2012]: (1) direct propagation of tides into the upper thermosphere and/or (2) indirectly through changes in the electric fields associated with wind modifications in the ionospheric dynamo region.

In this study we focus on the indirect coupling mechanism via electrodynamics and examine the changes in the neutral winds and low-latitude vertical $E \times B$ drift. The effect of changes in the vertical drift on the ionospheric density will form the basis for a separate study. The goal of the present study is to quantify the influence of different tidal and planetary wave (PW) components on the low-latitude vertical drift changes during a SSW period as simulated by the thermosphere-ionosphere-mesosphere electrodynamics general circulation model (TIME-GCM).

To quantify the SSW effects we examine the amplitudes of the different longitudinal wave numbers in the vertical drift at different local times, rather than decomposing the vertical drift into tidal harmonics with specific periods and zonal wave numbers. Tidal harmonics of the vertical drift components have limited utility, since they are produced by the combinations of multiple tidal neutral wind components from different latitudes and heights interacting with the strong diurnal and longitudinal variations of the ionospheric conductivity, and have a signature of the geomagnetic main field variation included. Therefore, we do not expect to see a one-to-one correspondence between harmonics of the neutral winds and of the vertical $E \times B$ drift.

Throughout this study the vertical drift components are expressed in longitudinal wave numbers, hereafter wn, at specific local times or local time bins, while all neutral wind components are specified by the zonal wave number s and frequency n (per day). Our wave naming convention is as follows. For the tidal components we use: D for diurnal ($n = 1$), S for semidiurnal ($n = 2$), and T for terdiurnal ($n = 3$), and eastward ($s < 0$) or westward ($s > 0$) propagating tides are denoted by E or W, respectively, with the zonal wave number s, e.g., DW1 is the diurnal westward propagating tide with zonal wave number 1. If $s = n$, the wave is called "migrating" since it is moving with the apparent motion of the Sun, e.g., DW1, SW2, and TW3. If the zonal wave number is $s = 0$, it is called a "standing" wave denoted by an S, e.g., DS0. Waves which do not have a period (frequency $n = 0$) are called stationary planetary waves with zonal wave number s e.g., PW1 for $s = 1$. At a particular universal time (UT), a wave can be observed with s maxima along a latitude circle, while from a fixed local time perspective, the observed longitudinal wave number (wn) is $|s - n|$.

The tidal spectrum during SSW periods can change, among other reasons, due to the changes in the background atmosphere, in the ozone distribution which forces tides in the middle atmosphere, or by nonlinear wave-tide and tide-tide interaction. *Liu and Roble* [2002] demonstrated the importance of gravity waves, planetary waves, the background atmosphere and tides, and their interplay by analyzing TIME-GCM simulations for a stratospheric warming event. In this study we focus on the tidal changes between approximately 70 and 130 km and do not examine what causes the neutral wind changes below. However, we are aware that some wave/tidal changes are due to the nonlinear interaction with the strong stationary planetary

wave and therefore happen even before the warming itself, while other changes might be attributed to the disturbed middle atmosphere. To emphasize that the warming peak does not cause all the dynamical changes we refer in the following to the "SSW period" or period with "strong planetary wave activity."

It has been known for a long time that lunar tides can produce lunar semidiurnal signatures that impact the ionosphere, e.g., in the ionospheric current, equatorial electrojet, and vertical plasma drift [e.g., *Stening*, 1986; *Stening and Fejer*, 2001]. Recently, the enhancement of the lunar semidiurnal tide during SSW event was observed in the ionospheric drifts, equatorial electrojet, and ground magnetic perturbations [e.g., *Fejer et al.*, 2010, 2011; *Park et al.*, 2012]. *Pedatella and Liu* [2013] demonstrated with numerical experiments using the TIME-GCM and results from the Whole Atmosphere Community Climate Model (WACCM) that the lunar tide can contribute up to 30% to the ionospheric SSW response. However, the magnitude and the sign of the lunar contribution depend on the phase of the lunar tide with respect to the SSW timing. *Pedatella and Liu* [2013] found that a phase shift of the SW2 tide is responsible for a significant part of the ionospheric changes leading to an increase in the vertical $E \times B$ drift in the morning and a decrease in the afternoon. This is aligned with the findings of *Fuller-Rowell et al.* [2010] who could reproduce the vertical drift and ionospheric signal for the 2009 SSW using the Whole Atmosphere Model (WAM) without including lunar tides. Lunar tides are not included in the present simulations. In a follow-on study we will pursue the comparative role of the lunar gravitational tide.

The paper is structured as follows. In section 2 we introduce the TIME-GCM used to simulate the 2006 SSW period. The SSW characteristics and the prevailing geospace conditions are described in section 3. The simulated ionospheric SSW signals are discussed in section 4. In section 5 we focus on the simulated low-latitude vertical drift changes and examine the causes of the wn1 and wn4 vertical drift changes in sections 5.1 and 5.2, respectively. We conclude the paper with a summary of the main findings in section 6.

2. Model Simulation

For this study we used the National Center for Atmospheric Research thermosphere-ionosphere-mesosphere electrodynamics general circulation model (TIME-GCM). The most important characteristics of the model are summarized below. The TIME-GCM is a three-dimensional, time-dependent general circulation model that simulates the dynamics, temperatures, composition, and electrodynamics of the middle and upper atmosphere, including the ionosphere, from first principles. The TIME-GCM is described by *Roble* [1995, 1996] and uses the electrodynamics as described by *Richmond and Maute* [2013]. The upper boundary ranges between 450 and 650 km, depending on the 10.7 cm solar radio flux ($F_{10.7}$), which is a model input. The O^+ flux and electron heat flux are prescribed at the upper boundary.

To simulate the geomagnetic variability for 2006 we used the 3-hourly *Kp* index to drive the high-latitude convection pattern from *Heelis et al.* [1982], and to calculate the hemispheric power of total particle precipitation. The studied January–March 2006 period was geomagnetically quiescent with low $F_{10.7}$ (average of 78 sfu (solar flux unit); 1 sfu = 10^{-22} W/m^2/Hz) and an average *Kp* of 1.5.

We perturbed the lower boundary of the TIME-GCM (i.e., approximately 30 km) with monthly tidal climatology as specified by the Global Scale Wave Model (GSWM-02) [*Hagan and Forbes*, 2002, 2003]. GSWM-02 provides tidal perturbations of the geopotential height, neutral temperature, and the zonal and meridional neutral winds. GSWM-02 includes eastward and westward propagating diurnal and semidiurnal tides with zonal wave number 0 to 6. The TIME-GCM background atmosphere at the lower boundary is specified by daily averaged European Centre for Medium-Range Weather Forecasts (ECMWF) data of the geopotential height, the neutral temperature, and the horizontal neutral winds. Using daily averaged ECMWF data ensures that the tides are solely specified by the GSWM-02, while the background atmosphere and the planetary waves associated with the 2006 SSW are quantified by the ECMWF data.

A consequence of using daily averaged ECMWF data with tidal climatology given by GSWM-02 is that we neglect plausible SSW changes in the tidal components originating below 30 km. Although these might have an effect, the advantage of using tidal climatology is that we can more easily delineate the tidal and planetary wave effects. We performed two TIME-GCM simulations with different lower boundary forcing: one includes and the other excludes planetary wave forcing with the background atmosphere specified by the ECMWF data. In the following we will refer to the simulation with the ECMWF data at the lower boundary as the case "with planetary wave forcing" for short. The simulation using the default TIME-GCM seasonally

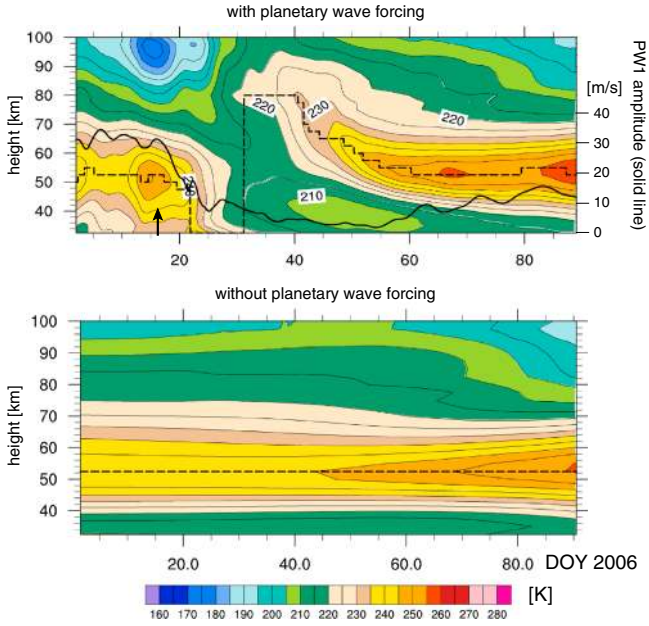

Figure 1. Zonal mean neutral temperature between 70° and 80° geographic latitude as simulated by TIME-GCM (top) with and (bottom) without planetary wave activity at the lower boundary. The maximum temperature in height is indicated by the dashed black line (left *y* axis), and the average PW1 amplitude of the zonal wind (m/s) between 70° and 80° geographic latitude at 32.5 km is illustrated by the solid black line (right *y* axis); the black arrow at day of year (DOY) 16 indicates the time after which the Northern Hemisphere polar PW1 amplitude is decreasing.

varying empirical background atmosphere we refer to as "without planetary wave forcing" or the "base case." The comparison of the two simulations enables us to quantify the effects of the strong January 2006 planetary wave activity and the associated SSW on the middle atmosphere, the lower thermosphere, and the electrodynamics.

3. The 2006 SSW

The evolution and characteristics of the 2006 SSW period in the stratosphere and lower mesosphere are described by, e.g., *Manney et al.* [2008], *Smith et al.* [2009], and *Siskind et al.* [2010] and are briefly summarized in the following. The 2006 SSW is caused by a stationary planetary wave 1 (PW1) in the northern polar stratosphere. Its temporal evolution is shown by the solid black line in Figure 1 (top). The stratospheric PW1 was already large in December with further enhancement in January. Between days 5 and 10, and after day 16, a stationary planetary wave with zonal wave number 2 (PW2) was enhanced due to the distortion of the polar vortex [*Manney et al.*, 2008]. The strong stratospheric planetary wave activity led eventually to a sudden warming in the stratosphere, and a reversal of the zonal mean zonal wind at 60° geographic latitude and 10 hPa on 21 January [*Manney et al.*, 2008].

The SSW in January 2006 is characterized as a major, prolonged event. *Smith et al.* [2009] analyzed Sounding of the Atmosphere using Broadband Emission Radiometry (SABER) nighttime neutral temperatures averaged between 70°N and 83°N showing the disappearance of the warm temperatures at approximately 50 km at day 25, the reformation of the temperature peak at 80 km 5 days later, and the long recovery phase lasting till the end of March. The SABER neutral temperature variation agrees well with the evolution of the stratopause in the TIME-GCM shown in Figure 1 (top), with the same discontinuity and long recovery phase as shown by *Smith et al.* [2009]. This confirms that our simulated background atmosphere is realistic, which is important because the tidal and wave propagation depends, among other things, on the background conditions. Without planetary wave forcing at the lower boundary (Figure 1, bottom), the stratopause is very stable at approximately 50 km, and the temperature changes are due to the seasonal variation.

4. Signals of SSW in the Ionosphere

Goncharenko and Zhang [2008] first reported on the link between stratospheric changes and ionospheric variability during the 2008 SSW period. In a later study, *Goncharenko et al.* [2010a] observed 50–100% GPS

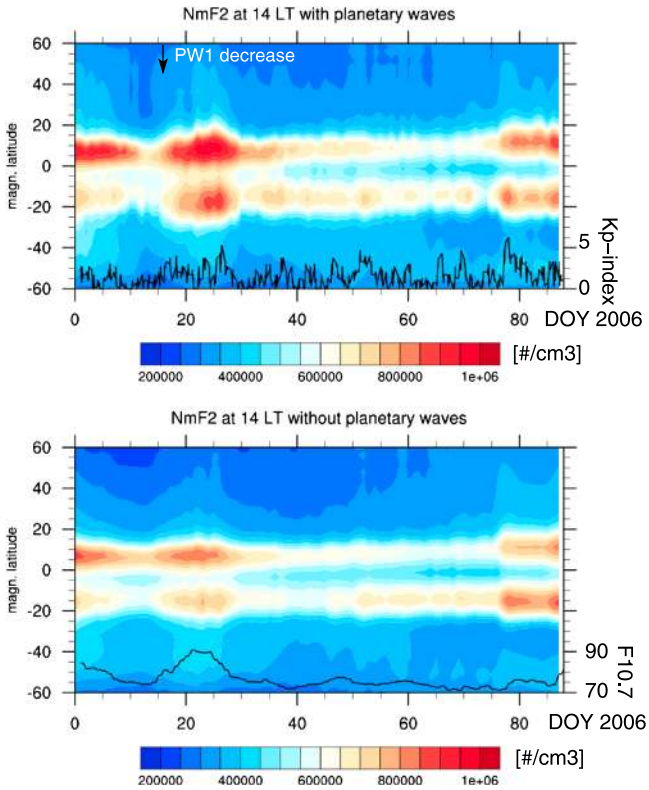

Figure 2. Peak electron density in the *F* region (NmF2) (#/cm^3) as simulated by the TIME-GCM for 14 LT and 0° geographic longitude (top) with and (bottom) without planetary wave forcing; the 3-hourly *Kp* and the daily $F_{10.7}$ radio flux (10^{-22} W m^{-2} Hz^{-1}) variations are indicated by the black lines in Figures 2 (top) and 2 (bottom), respectively; the black arrow at DOY 16 indicates the time after which the Northern Hemisphere polar PW1 amplitude is decreasing.

total electron content (TEC) changes in the EIA region during the 2009 SSW. The general low-latitude ionospheric SSW signal is described as an enhancement of the EIA in the morning and a suppression in the afternoon, with a few days delay after the SSW warming [*Goncharenko et al.*, 2010b]. Correspondingly, the vertical equatorial drift shows an enhanced upward drift in the morning and a reduction in the afternoon [*Chau et al.*, 2009]. Several studies provided observational confirmation [e.g., *Anderson and Araujo-Pradere*, 2010; *Rodrigues et al.*, 2011; *Chau et al.*, 2010; *Goncharenko et al.*, 2010b; *Yue et al.*, 2010] and numerical support [e.g., *Fuller-Rowell et al.*, 2010, 2011; *Pedatella et al.*, 2012a; *Fang et al.*, 2012; *Jin et al.*, 2012; *Liu et al.*, 2013a] of this local time behavior.

In the following we focus on the peak *F* region electron density (NmF2) during January to March 2006 to examine the simulated ionospheric effect of the disturbed middle atmosphere. The NmF2 is shown in Figure 2 at 14 local time (LT) and 0° geographic longitude with planetary wave forcing in Figure 2 (top) and without it in Figure 2 (bottom). Including the planetary wave at the lower boundary increases the NmF2 and moves the equatorial ionization anomaly slightly more poleward. Analyzing the difference of the simulations reveals that from day 15 to day 30, the EIA NmF2 is increased between 20–60% at low latitudes while the enhancements are around 20% from day 30 to day 55 at 14 LT and 0° geographic longitude compared to the base case. The model shows larger changes in the Northern Hemisphere as compared to the Southern Hemisphere changes, which is similar to the TEC observations [*Goncharenko et al.*, 2010b]. The magnitude of the change is smaller than what was observed for the 2009 SSW but comparable to the 2008 SSW period when an approximately 60% change in EIA TEC was observed [*Goncharenko et al.*, 2010b]. The maximum change in the simulated NmF2 is at day 25, which is 4 days after the polar jet reversal and within 3–6 days of the observed ionospheric response time [*Goncharenko et al.*, 2010b].

Although this TIME-GCM simulation reproduced the observed global ionospheric features during SSW periods, the local time variation in NmF2 or TEC does not agree well with previously reported observations. The observations show an increase in TEC before noon and a decrease in the afternoon, corresponding to the observed increase in vertical drift before noon and a decrease in the afternoon [*Chau et al.*, 2009]. This local

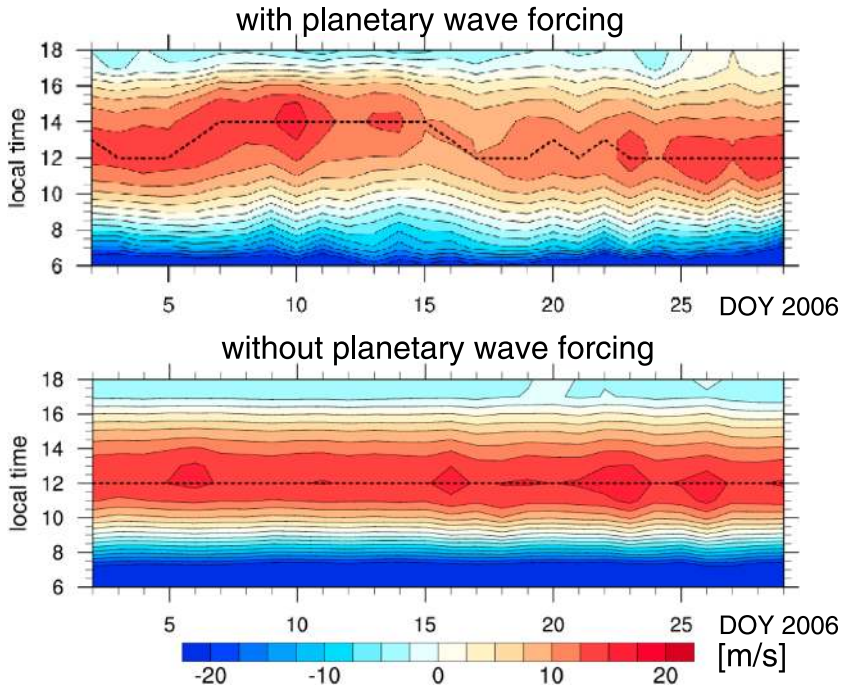

Figure 3. Simulated equatorial diurnal vertical $E \times B$ drift variation at 0° geographic longitude and 0° geomagnetic latitude versus DOY for the case (top) with and (bottom) without planetary wave forcing; the local time variation of the daytime vertical drift peak is depicted by the dashed line with a 1 h time resolution.

time change has been attributed to a change in the semidiurnal tide and the lunar tide [e.g., *Stening and Fejer*, 2001; *Fejer et al.*, 2010; *Forbes and Zhang*, 2012; *Pedatella and Liu*, 2013]. The present simulation does not include the effects of the lunar tides and uses climatological tidal forcing. Figure 3 depicts the equatorial diurnal vertical drift variation at 0° geographic longitude for the simulation with (Figure 3, top) and without (Figure 3, bottom) planetary wave forcing. In general, the daytime vertical drift peak occurs between noon and 14 LT for the case with planetary wave forcing, while quiet day observations and the base case exhibit the peak before [e.g., *Fejer and Scherliess*, 2001] and at noon, respectively. The reason for this difference is an approximately 1.5 h change in the migrating semidiurnal phase in the planetary wave forcing case which moves the daytime vertical drift peak to later local times. However, the daytime vertical drift peak is moving to earlier local times during the SSW period in the planetary wave forcing case, but not to 9–10 LT as observed at Jicamarca during the 2008 and 2009 SSW periods [*Chau et al.*, 2009, 2012]. Consequently, the diurnal NmF2 and TEC variations do not exhibit the observed strong increase before noon and decrease after noon. With planetary wave forcing the daytime vertical drift peak is reduced by approximately 2.5 m/s compared to the base case, which is opposite to what would be expected if only the strength of the equatorial plasma fountain changed. Other mechanisms than the fountain effect must exist to increase NmF2. Plausible mechanisms include reduced recombination due to changes in thermospheric composition or changes in the vertical or meridional wind fields. A detailed analysis is beyond the scope of the present study.

One of the suggested coupling process between the stratospheric changes and their ionospheric signals is a modified neutral wind system which couples to the ionosphere via the ionospheric wind dynamo. We depict representative quantities of the suggested coupling chain in Figure 4 for the January to March 2006 period as simulated by TIME-GCM. The panel shows the changes in the longitudinal variation for the low-latitude zonal wind at 110 km, the vertical $E \times B$ drift, and the NmF2 at 12 LT without (Figures 4a, 4d, and 4g) and with (Figures 4b, 4e, and 4h) planetary wave forcing. The zonal wind and the NmF2 are averaged between 0° and 16° geographic and geomagnetic latitude, respectively, to focus on the signal in the northern low-latitude region. The vertical $E \times B$ drift is averaged between −10° and 10° geomagnetic latitude. The temporal variation of the longitudinally averaged zonal wind, vertical $E \times B$ drift, and NmF2 at 12 LT is presented in Figures 4c, 4f, and 4i. Note that at a particular local time, the longitudinal average of the migrating tidal components does not vanish.

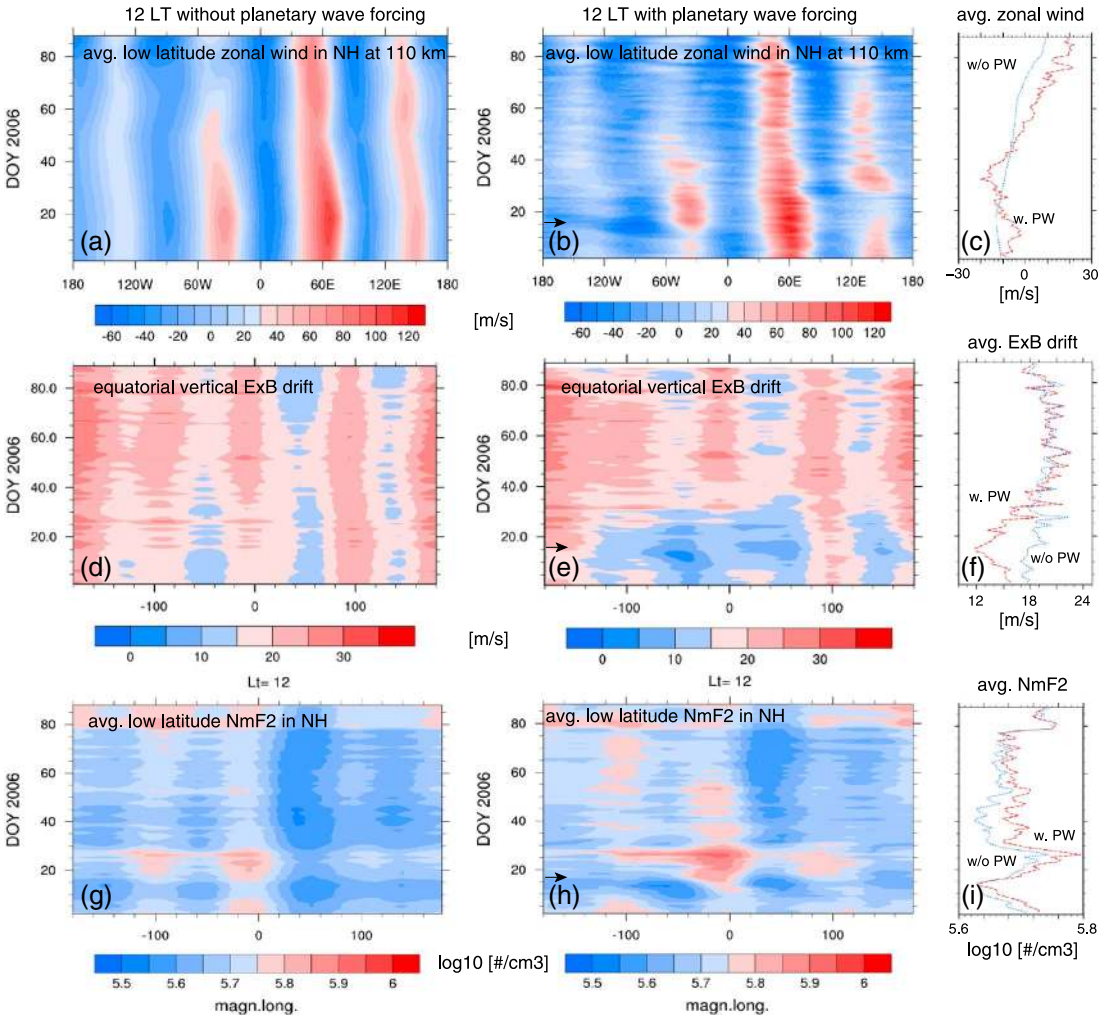

Figure 4. Variation in magnetic longitude and day of the year in the (a–c) zonal wind at 110 km (m/s) averaged between 0° and 16° geographic latitude, (d–f) equatorial vertical $E \times B$ drift (m/s) averaged between −10 and 10° magnetic latitude, and (g–i) F region peak electron density (NmF2) $\log_{10}$ (#/cm^3) averaged between 0° and 16° geomagnetic latitude as simulated by the TIME-GCM for 12 LT without planetary wave forcing (Figures 4a, 4d, and 4g) and with planetary wave forcing (Figures 4b, 4e, and 4h), and the longitudinal average for 12 LT (Figures 4c, 4f, and 4i) for zonal wind (m/s) (Figures 4a–4c), vertical $E \times B$ drift (Figures 4d–4f), and NmF2 (Figures 4g–4i); the black arrows at DOY 16 indicate the time after which the Northern Hemisphere polar PW1 amplitude is decreasing.

Due to the planetary wave forcing the temporal variability with timescales of days and longer increases especially for the zonal wind, and to a lesser extent for the vertical $E \times B$ drift and the NmF2. In the following we compare the longitudinal variation with and without planetary wave forcing for each quantity and find in general that the differences are largest in January.

The longitudinal four peak structure in the zonal wind at 110 km (Figure 4b) is already disturbed from day 1 of 2006 when the planetary wave 1 is strong (see Figure 1). The recovery from the disturbed middle atmosphere due to the SSW does not happen until approximately day 50–60 when the longitudinal structure of the simulation with planetary wave forcing approaches that of the base case. Note that the longitudinally averaged zonal wind at 12 LT is different for the whole January to March period.

In January the longitudinally averaged vertical drift at 12 LT with planetary wave forcing is up to 6 m/s smaller than without planetary wave forcing and exhibits the largest difference at the time of the stratospheric PW1 decrease (marked by the arrow in Figure 1) and the stratospheric warming. The vertical drift decrease is at least partly due to the phase shift in the migrating semidiurnal tide in the disturbed atmosphere, which moves the daytime peak in the case of planetary wave forcing to later local times (see Figure 3).

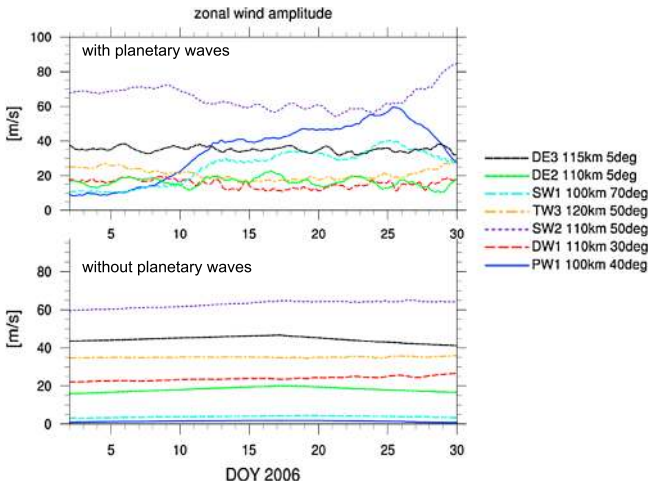

Figure 5. Temporal variation of zonal wind amplitude (m/s): PW1 at 100 km and 40° geographic latitude, DW1 at 105 km and 30° geographic latitude, SW2 at 110 km and 50° geographic latitude, TW3 at 120 km and 50° geographic latitude, SW1 at 100 km and 70° geographic latitude, DE2 at 110 km and 5° geographic latitude, and DE3 at 115 km and 5° geographic latitude (top) with and (bottom) without planetary wave forcing at the lower boundary.

In the disturbed ionosphere the daily maximum NmF2 is larger in January and February (DOY 1 to DOY 59) compared to the base case. And even during the moderate geomagnetic storm at day 27 ($Kp = 5$), the ionospheric response in NmF2 with planetary wave forcing is more intense than for the base case. This indicates that the SSW response in the NmF2 is still important during the minor storm. A control simulation (not shown here) with average January 2006 geomagnetic forcing confirms that the main signal in the ionosphere around day 27 is caused by the SSW and not by the geomagnetic activity. Based on the longitudinally averaged NmF2 (Figure 4i), it takes until day 70 for the ionosphere to recover from the SSW impacts. At 12 LT the recovery time in NmF2 is slower than in the vertical drift, which indicates that other mechanisms are present, e.g., possible in situ wind effects.

To better understand the changes in the vertical $E \times B$ drift in the simulations we first examine the tidal and PW components in the *E* region. Figure 5 shows some of the major tidal and PW zonal wind components at *E* region heights from the simulations with and without planetary wave forcing at Figures 5 (top) and 5 (bottom), respectively. We illustrate the various PW and tidal components at locations of large amplitudes. Their temporal evolution is described in the following and compared to published results.

First, the PW1 at 100 km and 40° geographic latitude is increased by over 30–50 m/s starting around day 10. Note that the midlatitude PW1 component at 100 km has a different time variation than the northern polar stratospheric PW1 (see Figure 1). The PW1 time variation will be examined and discussed in section 5.1.

The zonal wind amplitude of the migrating diurnal component (DW1) at 110 km and 30° geographic latitude decreases due to the planetary wave forcing by approximately 5–10 m/s. The meridional neutral wind component of DW1 (not shown here, around 25 m/s at 15° geographic latitude for the simulation with planetary wave forcing) agrees well with the simulation results from *Liu et al.* [2013b] for the 2006 SSW period (24 m/s at 10–12° geographic latitude). The zonal wind amplitude of the migrating semidiurnal (SW2) component averaged over January at 110 km and 50° increases slightly compared to the simulation without planetary wave forcing and has a negative correlation with the PW1 time variation at 110 km. A large SSW signal which correlates well with the *E* region midlatitude PW1 component can be seen in the westward propagating semidiurnal tide with zonal wave number 1 (SW1). The increase in the SW1 zonal wind amplitude is up to 35 m/s compared to the base case. The SW1 increase agrees with the statistical results from *Pedatella et al.* [2012a] using WACCM. The zonal wind amplitude of the eastward propagating diurnal tide with zonal wave number 2 (DE2) is not increasing with respect to the base case, but it is rather modulated. The magnitude of the DE2 amplitudes agrees with the modeling studies of, e.g., *Liu et al.* [2013b] and *Fuller-Rowell et al.* [2010].

The eastward propagating diurnal tide with zonal wave number 3 (DE3) zonal wind amplitude is approximately 10 m/s smaller at 115 km and 5° geographic latitude as compared to the base case. For the January–February 2006 SSW period *Liu et al.* [2013b] reported on an average simulated DE3 zonal wind

amplitude of 7 m/s with 3.5 m/s standard variation. In the present study the equatorial DE3 zonal wind amplitude is much larger with 35 m/s and 1.5 m/s standard deviation. *Talaat and Lieberman* [2010] using Wind Imaging Interferometer measurements reported on zonal wind amplitudes for a wave number 4 of 20 m/s in the *E* region which they interpreted as a DE3 component. *Oberheide and Forbes* [2008] developed a climatology based on Hough Mode Extension and using SABER and Thermosphere Ionosphere Mesosphere Energetics and Dynamics (TIMED) Doppler Interferometer (TIDI) measurements with DE3 zonal wind amplitudes of approximately 6 m/s in January at 100 km. *Hagan et al.* [2009] studied the September middle and upper atmosphere with TIME-GCM using GSWM-02 climatology at the lower boundary and noted that the DE3 component is around 50% larger than observed, which can be attributed to the overestimation of DE3 in GSWM-02, but they also suggested that tidal dissipation in the TIME-GCM upper mesosphere and lower thermosphere may be underestimated. The DE3 component in GSWM-02 is overestimated in the January to March time period compared to CHAMP observations [*Häusler et al.*, 2010]. The influence of the increased DE3 amplitude that characterizes our findings will be discussed in section 6.

Recently, *Fuller-Rowell et al.* [2010] reported on a significantly increased terdiurnal migrating tidal component (TW3) during a self-simulated minor SSW with the Whole Atmosphere Model (WAM). Since we will not discuss the TW3 tide in connection with the vertical drift, we briefly digress to compare the simulations with respect to the TW3 tide. The findings of *Fuller-Rowell et al.* [2010] contradict the decrease TW3 amplitude in the TIME-GCM simulation with planetary wave forcing. The difference in TW3 cannot entirely be attributed to the differences in the SSW characteristics. The amplitude of the TW3 in the midlatitude 100–150 km region in WAM is around 15–20 m/s before the SSW event, which is smaller than in the present base simulation, but similar to the magnitude of our TW3 of the planetary wave forcing case with 25 m/s at the beginning of January. During the warming event, a 50% (approximately 10 m/s) increase of the TW3 amplitudes is observed in WAM [*Fuller-Rowell et al.*, 2010] compared to a 10 m/s decrease in the TIME-GCM.

Smith and Ortland [2001] examined, among other things, the origin of the TW3 tidal component and found that it is mainly forced by solar heating in the middle atmosphere and that nonlinear tidal interaction between DW1 and SW2 being strongest at low latitudes plays a secondary role. Analyzing the time evolution of the height variations of the TIME-GCM tides suggest that the DW1 and SW2 tides interact in the middle atmosphere to generate a component of the TW3 tide. The decrease in the TW3 amplitude in TIME-GCM might be due to nonlinear interaction of DW1 with other tidal and wave components, e.g., DW1+PW1 and DW1+DE3, with DW1 losing momentum and energy, and rendering it unable to generate the larger TW3 component associated with the base case simulation. This is supported by the fact that DW1 is comparatively weaker during January in the case of planetary wave forcing.

5. Causes of the Vertical $E \times B$ Drift Changes

In this section we examine the importance of the neutral wind variations in generating the low-latitude daytime vertical $E \times B$ drift changes as simulated by TIME-GCM. As can be seen in Figure 4, the longitudinal variation of the low-latitude vertical $E \times B$ drift is disturbed during January (DOY 1 to DOY 30). We first determine the temporal variation of particular longitudinal wave number (wn) amplitudes in the low-latitude vertical $E \times B$ drift at specific local times via Fourier analysis. For example, to get the average low-latitude amplitudes of the vertical $E \times B$ drift waves at 12 LT in Figure 4, a Fourier analysis was performed for each day and each magnetic latitude between −10° and 10°. The latitudinal averaging has no significant influence on the result, indicating that the vertical $E \times B$ drift varies little between −10° and 10° magnetic latitude. The local time bins for extracting the longitudinal wave number in vertical $E \times B$ drift are selected such that changes in the longitudinal wave number amplitude are maximum. The vertical drift amplitudes are averaged over the local time bin. We focus on wave numbers 1 (wn1) to 4 (wn4) since ionospheric changes up to wave number 4 have been reported [e.g., *Immel et al.*, 2006; *Kil et al.*, 2007; *Lin et al.*, 2007; *England*, 2012].

Figure 6 depicts the resultant latitudinal and local time averaged amplitude of the January vertical $E \times B$ drift for wn1 to wn4. The strongest SSW signal can be found in wn1 between 12 and 15 LT. Starting around day 15, the increase in vertical $E \times B$ drift wn1 amplitude is up to 5 m/s compared to the base case (blue curve). The increase coincides with the time of the stratospheric polar PW1 decrease and the warming in the stratosphere. The wn2 amplitude in the 14–16 LT bin increases by approximately 3 m/s compared to the base case (Figure 6, top right) and peaks at day 15. The amplitude change in the 10–12 LT bin in the wn3 vertical $E \times B$ drift is around 1.5 m/s, and smaller than the wn1 and wn2 changes, but has a similar

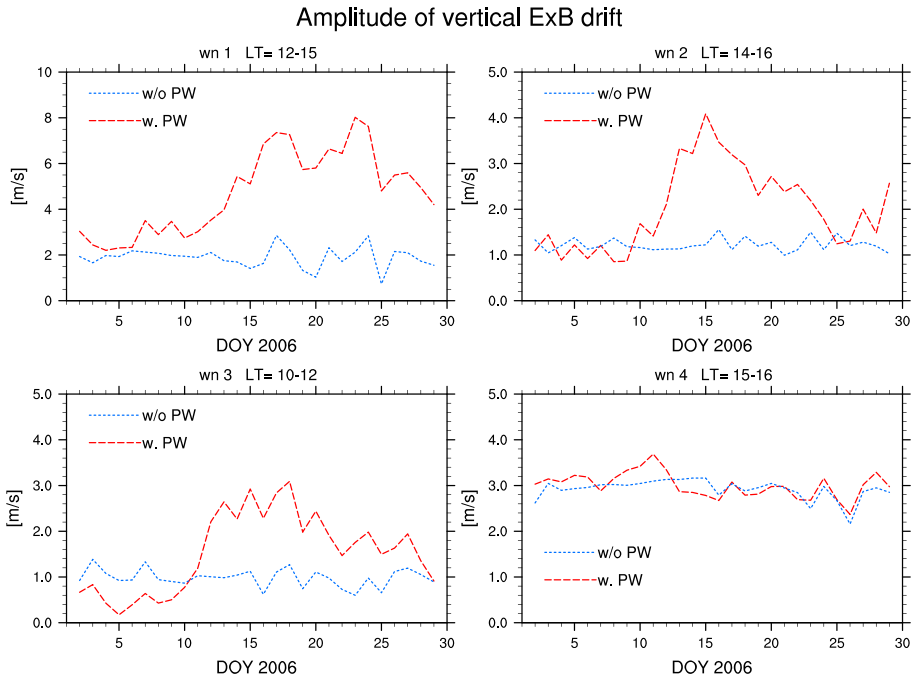

Figure 6. Amplitude of vertical $E \times B$ drift averaged between −10° and 10° geomagnetic latitude with planetary wave forcing (red dashed line), without planetary wave forcing (blue dotted line): (top left) wn1 for 12–15 LT, (top right) wn2 for 14 to 16 local time, (bottom left) wn3 for 10–12 local time, and (bottom right) wn4 for 11-13 local time.

temporal variation peaking around day 15 and remaining high till day 20. The exception in the temporal variation is the wn4 amplitude. A SSW signal can neither be seen in the 15–16 LT bin nor at other local times (not shown here).

The vertical $E \times B$ amplitude changes contribute to the variability in the vertical $E \times B$ drift in the corresponding local time bin. At local noon the vertical drift variability is around 35% of the average vertical $E \times B$ drift between day 12 and 20, while without planetary wave forcing, the variability is only 18% of the corresponding average vertical $E \times B$ drift. This is larger than the simulated variability of 16% by *Liu et al.* [2013b] over Jicamarca, Peru, using TIME-GCM nudged with WACCM/Modern-Era Retrospective Analysis for Research and Applications (MERRA) results for the 2006 SSW period. The different magnitude might be caused by the geomagnetic and the longitudinal variability which are accounted for in the present study. If we assume that the longitudinal and geomagnetic variability is similar for the simulation with and without planetary wave forcing, and that to a first approximation the longitudinal and geomagnetic variability is linear, we can then attribute the difference of the variability of the case with and without planetary waves to the planetary wave activity. The estimate of 17% for the variability due to the planetary wave activity in the present study compares favorably with the finding of *Liu et al.* [2013b].

To study the effects of certain wave and tidal neutral wind components on the vertical $E \times B$ drift, we solve the standard ionospheric electrodynamo equation [see *Maute et al.*, 2012, equation (1)] as a postprocessing step without any feedback to the thermosphere-ionosphere system. We include a limited number of nonmigrating tidal and PW components of the neutral wind forcing in the electrodynamo equation but always include the background neutral wind as well as the migrating diurnal, semidiurnal and terdiurnal tidal components. The geomagnetic main field, the conductivities, and the high-latitude ion convection patterns are identical with the self-consistent simulation. We neglect the electric fields generated by the plasma pressure gradient and gravity-driven ionospheric current since our focus is on the influence of the neutral winds. This ionospheric current was included in the self-consistent simulations, but its influence is negligible during the day [e.g., *Eccles*, 2004; *Maute et al.*, 2012]. The electric potential is calculated every 10 min.

5.1. Wave Number 1 Amplitude in the Vertical $E \times B$ Drift

The simulated changes in the wn1 vertical drift amplitude are the largest and are discussed in this section. The most likely cause of the wn1 amplitude variation in January is the change in the neutral wind, as seen in

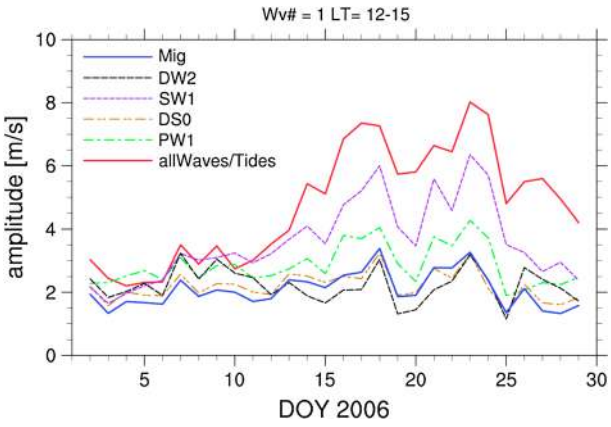

Figure 7. The wn1 amplitude of vertical $E \times B$ drift averaged between −10° and 10° geomagnetic latitude and 12–15 LT for January 2006 for different wave components (all cases include the same background winds and migrating tides): total wind field (red, solid line), migrating components (blue, solid line), DW2 (black, long dashed), SW1 (purple short dashed), DS0 (brown, dash-double dotted), and PW1 (green, dash-dotted) components.

Figure 7, which shows the amplitude of the wn1 in the vertical $E \times B$ drift due to the different neutral wind components. A wn1 can be generated by a PW1, a diurnal standing tide (DS0), a diurnal westward propagating tide with zonal wave number 2 (DW2), and a semidiurnal westward propagating tide with zonal wave number 1 (SW1). We did not consider other tides with smaller periods and larger wave numbers since these have smaller amplitudes and are less effective in the ionospheric wind dynamo, e.g., TW2, TW4, and SW3. As a reference, we show in Figure 7 the case with only migrating tides and the case with all the wave and tidal components included in the neutral wind. The contribution of a specific component is the difference between the curve for the migrating case and the curve for that specific component.

The largest contribution to the wn1 vertical $E \times B$ drift variation associated with the SSW is from the SW1 (purple short dashed line) with almost 3 m/s, followed by the PW1 (green dash-dotted line) with approximately 1 m/s. Including the neutral wind components from DW2 (black long dashed line) and DS0 (brown dashed-double dotted line) does not significantly increase the wn1 amplitude compared to the migrating case (blue solid line).

We already saw in Figure 5 that both *E* region zonal wind amplitudes of SW1 and PW1 increased after day 10 compared to the base case. Figure 8 gives a more detailed picture by showing the zonal wind amplitude at 110 km of SW1 (Figure 8, top), PW1 (Figure 8, middle), and SW2 (Figure 8, bottom) for the simulation with (without) planetary wave forcing at the lower boundary in Figures 8 (right) and 8 (left), respectively. Without planetary wave forcing, there is a small increase in SW1 at high latitude of approximately 10 m/s (Figure 8, top left) due to ion-neutral coupling introduced by the offset of the geomagnetic and geographic pole [*Jones et al.*, 2013]. But in the case of planetary wave forcing, the amplitude increase is up to 40 m/s in the Northern Hemisphere and extends equatorward to 30° geographic latitude (Figure 8, top right).

Analyzing the latitudinal and height variations of the neutral wind PWs and tides over time indicates that the Northern Hemisphere SW1 increase is caused by the wave-tidal interaction of SW2 and PW1 around 90–100 km and poleward of approximately 75° geographic latitude [e.g., *Smith*, 2012]. The nonlinear tide-wave interaction generates a SW1 and SW3 component, as suggested by *Forbes et al.* [1995]. The decrease in the SW2 amplitude in the Northern Hemisphere provides evidence of this interaction.

It is also very interesting that a strong enhancement of SW1 (Figure 8, top right) of 25–35 m/s in the proximity of −60° geographic latitude is present in the Southern Hemisphere which seems to be anticorrelated with the SW2 temporal variation in the Southern Hemisphere. *Pedatella et al.* [2012a] reported on the SW1 enhancement in the Southern Hemisphere of about 50% of that in the Northern Hemisphere. It might be possible that the Southern Hemisphere SW1 increase is partly caused by the same nonlinear interaction between PW1 and SW2, which is supported by the fact that the simulated SW2 and SW1 temporal variations are anticorrelated. Another possibility of generating an additional SW1 component is due to the DW1 and DS0 interaction. *Pedatella et al.* [2012a] showed that in WACCM, the simulated meridional DS0 amplitude in the *E* region undergoes significant changes at −60° geographic latitude during SSW periods. Further studies are needed to examine SSW signals in the Southern Hemisphere.

The PW1 amplitude in Figure 8 (middle) at 110 km has a very complex latitudinal structure with distinct bands. In the polar region, the increase of PW1 is linked to the original PW1 activity in the stratosphere [*Liu and Roble*, 2002; *Smith*, 2003]. Analyzing the temporal evolution of the height structure of PW1 (not shown here) indicates that the PW1 enhancement around 40° to 60° geographic latitude is only partly due to the upward propagation of the planetary wave, and only weakly linked to the polar region. Tidal

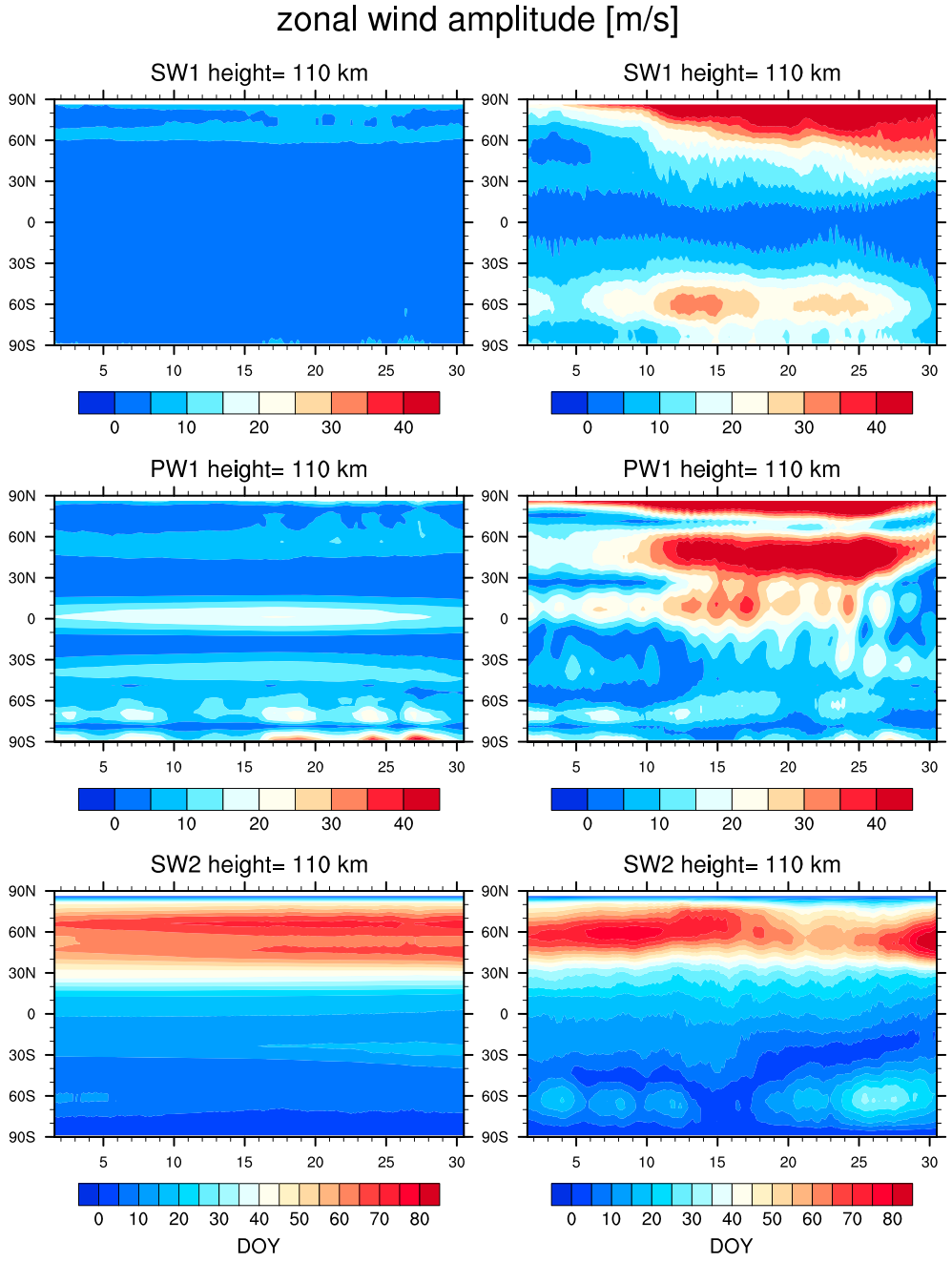

Figure 8. Zonal wind amplitude at 110 km for January (left) without planetary wave forcing and (right) with planetary wave forcing for (top) SW1, (middle) PW1, and (bottom) SW2 components.

and PW diagnostics which are not presented here suggest that the SW1 and SW2 tidal components at 95–105 km generate a PW1 around 40° to 60° geographic latitude. In the case of the simulation without planetary wave forcing, an enhancement of the PW1 amplitude (Figure 8, middle left) by 5–10 m/s can be seen at 50° to 60° geographic latitude which might be caused by the same nonlinear interaction of the SW2 and SW1 tidal components, only that the SW1 tidal component is much weaker at high latitudes resulting in a smaller PW1 component.

The third latitudinal band of PW1 amplitude is around the equator. The contribution from ion-neutral coupling generating a PW1 at the equator should not vary significantly during the month [*Jones et al.*, 2013]. The smooth temporal variation for the base case with a PW1 peak amplitude in the middle of January suggests that the nonlinear interaction between tidal components DE2 and DE3 generates the equatorial PW1

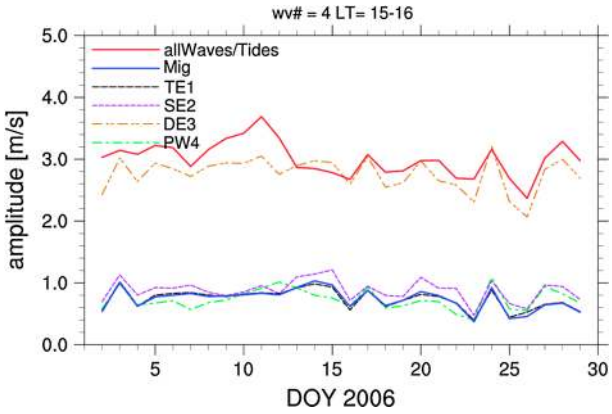

Figure 9. The wn4 amplitude of vertical $E \times B$ drift averaged between −10° and 10° geomagnetic latitude and 15–16 LT for January 2006 for different wave components (all cases include the same background winds and migrating tides): total wind field (red, solid line), migrating components (blue, solid line), TE1 (black, long dashed), SE2 (purple, short dashed), DE3 (brown, dash-double dotted), and PW4 (green, dash-dotted) components.

component. The equatorial PW1 amplitude of the simulation with planetary wave forcing has a higher day-to-day variation. In section 5.2, we will present results alluding to the connection of the temporal variation of the equatorial PW1 amplitude to that of DE2 and DE3.

We want to point out that the presented wave and tidal wind diagnostics are not able to explain why these different tidal and wave interactions happen in TIME-GCM. However, the TIME-GCM diagnostics can offer some insights into what the model suggests could be observed if wind observations became available. The TIME-GCM diagnostics cannot explain why the contribution of SW1 to the wn1 vertical drift is larger than that of the PW1 component although the maximum amplitudes at 100 km are similar. A possible cause might be the very different latitudinal structure. We did not examine the influence of the height and latitude variation, and/or of the meridional wind component. Further numerical testing would be needed to shed light on the relative importance of the SW1 and PW1 components. It is important to note that the component with the largest neutral wind amplitude in the *E* region is not necessarily the most efficient one in generating low-latitude vertical drift changes.

5.2. Wave Number 4 Amplitude in the Vertical $E \times B$ Drift

As shown in Figure 6, there is no SSW signal in the wn4 vertical $E \times B$ drift although SSW signals were found in wn1 to wn3. In the following we examine why the wn4 vertical drift response to the SSW is different. A wn4 in the vertical $E \times B$ drift at a specific local time can be produced by a DE3, SE2, TE1, or PW4 component. Several studies [*Hagan et al.*, 2009; *Oberheide et al.*, 2011; *Pedatella et al.*, 2012b] noted that, in addition to the DE3, PW4 and SE2 should be considered for the electrodynamic coupling between *E* and *F* region. We examine the influence of each of these PW and tidal components on the vertical drift in Figure 9 for the 15–16 LT bin. As for the wn1 amplitude, we neglect the components with higher zonal wave numbers or smaller periods, e.g., DW5 and SW6. Independent of the local time considered (not shown here), we find that DE3 is the major contributor to the wn4 in the daytime vertical $E \times B$ drift.

The temporal variation of DE3, SE2, and PW4 zonal wind amplitudes (Figure 5 (top) black line for DE3; SE2 and PW4 are not shown here) does not indicate a significant variation in January, in contrast to the temporal evolution of PW1 and SW1 zonal wind amplitudes. The SE2 and PW4 components are mainly generated through nonlinear interaction between DW1 and DE3 [*Hagan et al.*, 2009], and since DE3 does not exhibit a SSW signal, no SSW signal in SE2 and PW4 can be observed. The zonal wind amplitudes for PW4 and SE2 based on 2008 TIDI/TIMED measurements presented by *Oberheide et al.* [2011] are approximately 50% smaller than in this model study, which is probably due to the above mentioned overestimation of the simulated DE3 component.

In the following we focus on DE3 as the main contributor to the wn4 generation in the vertical drift. In Figure 5, the *E* region DE3 zonal wind amplitude is smaller in the simulation with planetary wave forcing than in the base case. Figure 10 illustrates the zonal wind amplitudes of DE2 (Figure 10, top), PW1 (Figure 10, middle), and DE3 (Figure 10, bottom) for the simulation with (without) planetary wave forcing in Figures 10 (right) and 10 (left), respectively. Without planetary wave forcing, the DE3 zonal wind amplitude varies smoothly in time and is almost 10 m/s larger than for the case with planetary wave forcing. The model results suggest that the DE3 is weakened because of the nonlinear interaction with the equatorial PW1 at 70–80 km altitude, which generates a DE2 and a DE4 component. Since in the simulated low-latitude mesosphere, PW1 is strong all through January (see Figure 10, middle right), there is no strong temporal variation associated with the SSW in the DE3 component.

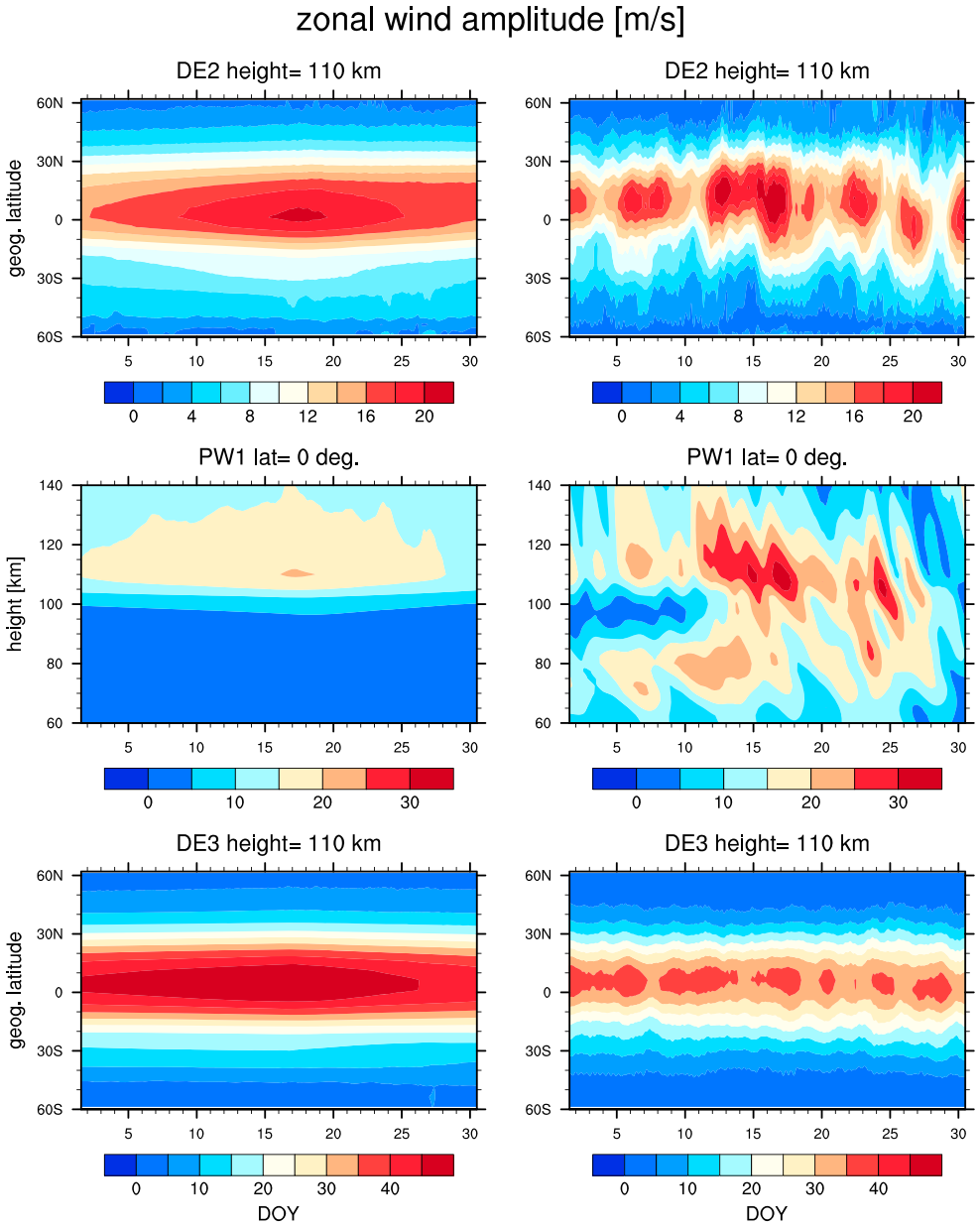

Figure 10. Zonal wind amplitude for (top) DE2 at 110 km, (middle) PW1 at 0° geographic latitude, and (bottom) DE3 at 110 km for the simulation (right) with and (left) without planetary wave forcing.

The DE2 zonal wind amplitude is shown at 110 km in Figure 10 (top). Without planetary wave forcing, the DE2 amplitude varies smoothly over the month of January, with a peak in the middle of the month which is associated with the GSWM-02 monthly climatology at the lower boundary. Adding planetary waves at the lower boundary does significantly change the temporal variation and latitudinal structure of the DE2 zonal wind amplitude. The model results indicate that one possible source of the additional DE2 variation without a change in magnitude is the modulation of the upward propagating DE2 component due to the nonlinear interaction between DE3 and PW1.

Further, the model diagnostics suggest that a second mechanism might take place weakening the DE3 component. In the equatorial *E* region, the DE3 and DE2 components are still strong. The height variation of PW1 (Figure 10, middle right) depicts larger amplitudes around approximately 70–90 km and a second increase in the PW1 amplitude from 110 km upward, which can only partly be explained by an upward propagating PW1 component. The strong correlation in the temporal variability of the PW1 and the DE2 amplitudes

around 110 km in the simulation indicates that the nonlinear interaction between DE3 and DE2 could generate an equatorial PW1 component. The same nonlinear interaction between DE3 and DE2 takes place in the simulation without planetary wave forcing, probably leading to the slight PW1 amplitude peak (Figure 10, middle left) in the middle of January which coincides with the time of the DE2 and DE3 peak amplitudes. This second nonlinear interaction might additionally weaken the DE3 component.

The suggested nonlinear interactions do not explain why the wn4 in the vertical drift with planetary waves in the 15–16 LT bin is similar in magnitude to the base case (see Figure 6), even though the DE3 zonal wind amplitude is smaller for the case with planetary wave forcing. We examined the local time variation of the wn4 amplitude in the vertical $E \times B$ drift for both simulations (not shown here). The base simulation has the largest wn4 amplitude in the vertical $E \times B$ drifts around 12–13 LT, while for the case with planetary wave forcing, the maximum wn 4 amplitude is shifted to later local time, around 15–16 LT. This 3 h local time shift cannot be explained alone by the difference in the DE3 phase of approximately 1.5 h. In addition, the SW2 experiences an average phase shift of approximately 1.5 h in January due to the planetary wave forcing, which leads to a shift of the daytime vertical $E \times B$ drift peak to later local times (see Figure 3).

We conducted a numerical experiment to confirm that in the model, the local time of the maximum wn4 amplitude due to DE3 depends on the local time of the daytime vertical drift peak, i.e., the phase of the SW2. We used the identical DE3 neutral wind component from the simulation with planetary wave forcing combined with either the SW2 neutral wind component from the base case or the SW2 component from the planetary wave forcing case. In the base case, SW2 phase is shifted by approximately 1.5 h to earlier local times, and the peak of the wn4 vertical drift amplitude moves to earlier local times, too, even though an identical DE3 tidal component was used. This confirms that in the simulation with planetary wave forcing, the phase shifts in the SW2 and in the DE3 neutral wind components are mainly responsible for the shift of the wn4 amplitude maximum to later local times.

The DE3 behavior described in the previous section explains why the wn4 magnitude in the vertical $E \times B$ drift at 15–16 LT is similar in magnitude for the planetary wave forcing case and the base case (Figure 6) even though the DE3 amplitude is reduced due to the presence of a planetary wave. This decrease is offset by the SW2 phase shift which moves the daytime vertical drift peak to later local times, and a correspondingly larger wn4 vertical drift amplitude at later local times is generated. As expected, the magnitude of the wn4 vertical drift amplitude of the base simulation at 11–13 LT (not shown here) is 1 m/s larger than for the simulation with planetary wave forcing.

We briefly summarize below the causes for the amplitude changes in the wn2 and wn3 as simulated by TIME-GCM and shown in Figure 6. The amplitude changes in wn2 in the vertical $E \times B$ drift is mainly caused by a PW2 which contributes approximately 1.5 m/s and a semidiurnal standing tide (SS0) with a roughly 0.5 m/s contribution. The weak SSW signal of 1.5 m/s in the wn3 in the vertical $E \times B$ drift can be attributed to changes in the planetary wave with zonal wave number 3 (PW3) (1 m/s) and the eastward propagating semidiurnal tide with zonal wave number 1 (SE1) (0.5 m/s).

6. Summary

In this study we quantified the TIME-GCM changes in the low-latitude vertical $E \times B$ drift associated with specific tidal and PW neutral wind components due to a realistic daily varying background atmosphere with planetary wave specification at the lower boundary representative of January 2006 conditions. The main findings are summarized in the following:

1. TIME-GCM can simulate the disturbed middle atmosphere during the prolonged 2006 SSW period as observed by SABER [*Smith et al.*, 2009]. Simulating a realistic background atmosphere is important since the wave and tidal propagation is influenced by the background atmosphere.
2. Due to the planetary wave forcing at the lower boundary, the NmF2 in the EIA region at 14 LT is increased by 20–60% between days 15 and 30. From days 30 to 55, the NmF2 enhancements are approximately 20%. The magnitude of the changes is consistent with the observed TEC changes during the 2008 SSW event [*Goncharenko et al.*, 2010b]. The NmF2 peak in the EIA region moves to higher latitudes. The peak increase in the NmF2 occurs 4 days after the polar jet reversal, agreeing with the observed delay in the ionospheric response of 3–6 days [*Goncharenko et al.*, 2010b]. The low-latitude vertical $E \times B$ drift variability

between days 12 and 20 increases from 18% to 35% at 12 LT due to the planetary wave activity at the lower boundary, which is similar to the findings of *Liu et al.* [2013b].

3. The strongest SSW low-latitude vertical $E \times B$ drift response in the simulation was found in the wn1 component, with an increase of up to 5 m/s, which contributes to the ionospheric variability. Numerical tests showed that this increase is mainly caused by the SW1 neutral wind tide (approximately contributing 3 m/s) and the PW1 component (contributing roughly 1 m/s). The SW1 neutral wind component in the Northern Hemisphere is increased due to the nonlinear interaction between SW2 and PW1 in the high-latitude polar region around 90–100 km [see *Smith*, 2012, and references therein]. TIME-GCM results suggest that the reverse nonlinear interaction between SW1 and SW2 around 95–105 km at midlatitude generates a PW1 component which peaks between 50° and 60° geographic latitudes. This is to our knowledge the first evidence of this nonlinear interaction. These interactions can explain the weakening of the SW2 component in the *E* region, which is correlated to the strengthening of the SW1 and PW1 components. The simulation indicates that the contributions from the DS0 and DW2 neutral wind components to the wn1 in the low-latitude vertical $E \times B$ drift is negligible. The SSW signal in the wn1 vertical $E \times B$ drift is strong because SW1, which is the major driver, is generated by the enhanced winter polar PW1 component interacting with SW2.
4. No SSW signal was found in the wn4 component of the low-latitude $E \times B$ drifts in TIME-GCM. Numerical experiments showed that the wn4 is largely attributable to the DE3 neutral wind tide, confirming suggestions of, e.g., *Immel et al.* [2006], *Hagan et al.* [2007], and *Pedatella et al.* [2008] and that the SE2 and PW4 contributions are negligible. The DE3 zonal wind amplitude in the *E* region is decreased by 5–10 m/s in January due to the planetary wave activity. The model results indicate that in the mesosphere, DE3 interacts nonlinearly with the PW1 component at low latitudes to generate a DE2 component, which will modulate the upward propagating component of DE2. The strong temporal variation in the DE2 component, which is similar to the variation of the DE3 and PW1, supports the mechanism of the nonlinear interaction between PW1 and DE3. At *E* region heights and low latitudes, the TIME-GCM results indicate that the DE3 and DE2 components generate an equatorial PW1 component. The similarity between the temporal variations of the DE2 and PW1 zonal wind amplitudes in the *E* region indicates the presence of this mechanism. The nonlinear interactions between both DE3 and DE2, and between DE3 and PW1, can decrease and/or module the DE3 component. At mesospheric/lower thermospheric heights and low latitudes, all of these components (DE3, DE2, and PW1) are present from the beginning of January, and further, they do not exhibit a SSW signal during January. Therefore, the wn4 of the low-latitude vertical $E \times B$ drifts does not have a strong temporal variation due to the SSW.
5. The TIME-GCM local time variation of the low-latitude vertical drift does not capture the observation that the daytime peak moves to prenoon local times during the SSW but rather reveals peaks between noon and 13 LT. One reason is that the modeled SW2 zonal wind phase at 110 km is shifted by approximately 1.5 h to later local times, moving the daytime vertical $E \times B$ drift peak to later local times in the case of the planetary wave forcing. Surprisingly, this shift of the daytime vertical drift maximum also influences the local time of the peak in the wn4 vertical drift amplitude. Numerical experiments show that the maximum of wn4 vertical $E \times B$ drift will occur later in local time if the SW2 has a phase shift to later local time. Therefore, in the simulation with planetary wave activity, the wn4 peak occurs later in local time than in the base case. Further studies are needed to better understand this behavior.
6. In the TIME-GCM simulation, a TW3 is generated internally by direct solar forcing and nonlinear interaction between DW1 and SW2 [*Smith and Ortland*, 2001]. Contrary to the results of *Fuller-Rowell et al.* [2010], who reported a 50% increase in the TW3 amplitude during the SSW period, the TIME-GCM results indicate a decrease in the TW3 amplitude in the *E* region. The TIME-GCM DW1 and SW2 neutral wind tides exhibit a decreased amplitude during the SSW period, which may explain the decreased TW3 amplitude in our January simulation. The results suggest that DW1 might be weaker due to nonlinear interaction with the PW1 generating a DW2 in the lower atmosphere [*Hagan and Roble*, 2001]. The SW2 amplitude might be reduced due to the nonlinear interaction with PW1 around 90–100 km in the polar region. The possibility that a modification in stratospheric ozone contributes to the TW3 modification remains and is beyond the purview of our report.

Using the GSWM-02 tidal climatology in the TIME-GCM lower boundary forcing leads to an overestimation of the DE3 zonal wind component in the *E* region by a factor of about 50% compared to, e.g., *Oberheide and Forbes* [2008], *Talaat and Lieberman* [2010], and *Liu et al.* [2013b]. A smaller DE3 forcing would lead to

a smaller wn4 component in the simulated vertical $E \times B$ drift. The model results suggest that the relative importance of the tidal contributions from PW4, SE2, DE3, and TE1 to the wn4 amplitude in the vertical $E \times B$ drift may still be valid since all of these components with the exception of SE2 are generated through nonlinear interactions of DE3 with another wave or tide. PW4 is generated by the nonlinear interaction between DW1 and DE3 [*Hagan et al.*, 2009]. The same nonlinear interaction also generates a SE2 component; however, SE2 also has a tropospheric contribution [*Hagan and Forbes*, 2002; *Oberheide et al.*, 2007]. The SE2 component is most likely smaller than the DE3 component and more antisymmetric about the equator, and therefore less effective in the generation of the vertical $E \times B$ drift [*Forbes et al.*, 2008; *Oberheide et al.*, 2011].

This modeling study provides a perspective about the importance of the different tidal and wave components in attributing to the vertical $E \times B$ drift changes in the presence of a strong and persistent planetary wave with zonal wave number 1 and a stratospheric sudden warming.

Acknowledgments
A.M. and A.R. were supported in part by NASA grants X13AF77G and NNX09AN57G and by NSF grant AGS1138784. A.M. would like to thank Hanli Liu and Nicholas Pedatella for their helpful discussions. The National Center for Atmospheric Research is sponsored by the National Science Foundation.

Robert Lysak thanks the reviewers for their assistance in evaluating this paper.

References

Anderson, D., and E. A. Araujo-Pradere (2010), Sudden stratospheric warming event signatures in daytime $E \times B$ drift velocities in the Peruvian and Philippine longitude sectors for January 2003 and 2004, *J. Geophys. Res.*, *115*, A00G05, doi:10.1029/2010JA015337.

Chau, J., B. G. Fejer, and L. P. Goncharenko (2009), Quiet variability of equatorial $E \times B$ drifts during a sudden stratospheric warming event, *Geophys. Res. Lett.*, *36*, L05101, doi:10.1029/2008GL036785.

Chau, J., L. P. Goncharenko, B. G. Fejer, and H.-L. Liu (2012), Equatorial and low latitude ionospheric effects during sudden stratospheric warming events, *Space Sci. Rev.*, *168*, 385–417, doi:10.1007/s11214-011-9797-5.

Chau, J. L., N. A. Aponte, E. Cabassa, M. P. Sulzer, L. P. Goncharenko, and S. A. González (2010), Quiet time ionospheric variability over Arecibo during sudden stratospheric warming events, *J. Geophys. Res.*, *115*, A00G06, doi:10.1029/2010JA015378.

Eccles, J. V. (2004), The effect of gravity and pressure in the electrodynamics of the low-latitude ionosphere, *J. Geophys. Res.*, *109*, A05304, doi:10.1029/2003JA010023.

England, S. (2012), A review of the effects of non-migrating atmospheric tides on the Earth's low-latitude ionosphere, *Space Sci. Rev.*, *168*, 211–236, doi:10.1007/s11214-011-9842-4.

Fang, T.-W., T. Fuller-Rowell, R. Akmaev, F. Wu, H. Wang, and D. Anderson (2012), Longitudinal variation of ionospheric vertical drifts during the 2009 sudden stratospheric warming, *J. Geophys. Res.*, *117*, A03324, doi:10.1029/2011JA017348.

Fejer, B., and L. Scherliess (2001), On the variability of *F* region vertical plasma drifts, *J. Atmos. Sol. Terr. Phys.*, *63*, 893–897.

Fejer, B., M. E. Olson, J. L. Chau, C. Stolle, H. Lühr, L. P. Goncharenko, K. Yumoto, and T. Nagatsum (2010), Lunar-dependent equatorial ionospheric electrodynamic effects during sudden stratospheric warmings, *J. Geophys. Res.*, *115*, A00G03, doi:10.1029/2010JA015273.

Fejer, B. G., B. D. Tracy, M. E. Olson, and J. L. Chau (2011), Enhanced lunar semidiurnal equatorial vertical plasma drifts during sudden stratospheric warmings, *Geophys. Res. Lett.*, *38*, L21104, doi:10.1029/2011GL049788.

Forbes, J. M., and X. Zhang (2012), Lunar tide amplification during the January 2009 stratosphere warming event: Observations and theory, *J. Geophys. Res.*, *117*, A12312, doi:10.1029/2012JA017963.

Forbes, J. M., N. A. Makarov, and Y. I. Portnyagin (1995), First results from the meteor radar at south pole: A large 12-hour oscillation with zonal wavenumber one, *Geophys. Res. Lett.*, *22*(23), 3247–3250, doi:10.1029/95GL03370.

Forbes, J. M., X. Zhang, S. Palo, J. Russell, C. J. Mertens, and M. Mlynczak (2008), Tidal variability in the ionospheric dynamo region, *J. Geophys. Res.*, *113*, A02310, doi:10.1029/2007JA012737.

Fuller-Rowell, T., F. Wu, R. A. Akmaev, T.-W. Fang, and E. A. Araujo-Pradere (2010), A whole atmosphere model simulation of the impact of a sudden stratospheric warming on thermosphere dynamics and electrodynamics, *J. Geophys. Res.*, *115*, A00G08, doi:10.1029/2010JA015524.

Fuller-Rowell, T., R. Akmaev, F. Wu, T.-W. Fang, M. Iredell, and A. Richmond (2011), Forecasting the dynamic and electrodynamic response to the January 2009 sudden stratospheric warming, *Geophys. Res. Lett.*, *38*, L13102, doi:10.1029/2011GL047732.

Goncharenko, L., and S.-R. Zhang (2008), Ionospheric signatures of sudden stratospheric warming: Ion temperature at middle latitude, *Geophys. Res. Lett.*, *35*, L21103, doi:10.1029/2008GL035684.

Goncharenko, L., J. L. Chau, H.-L. Liu, and A. J. Coster (2010a), Unexpected connections between the stratosphere and ionosphere, *Geophys. Res. Lett.*, *37*, L10101, doi:10.1029/2010GL043125.

Goncharenko, L., A. J. Coster, J. L. Chau, and C. E. Valladares (2010b), Impact of sudden stratospheric warmings on equatorial ionization anomaly, *J. Geophys. Res.*, *115*, A00G07, doi:10.1029/2010JA015400.

Hagan, M., and J. Forbes (2003), Migrating and nonmigrating semidiurnal tides in the upper atmosphere excited by tropospheric latent heat release, *J. Geophys. Res.*, *108*(A2), 1062, doi:10.1029/2002JA009466.

Hagan, M. E., and J. M. Forbes (2002), Migrating and nonmigrating diurnal tides in the middle and upper atmosphere excited by tropospheric latent heat release, *J. Geophys. Res.*, *107*(D24), 4754, doi:10.1029/2001JD001236.

Hagan, M. E., and R. G. Roble (2001), Modeling diurnal tidal variability with the National Center for Atmospheric Research thermosphere-ionosphere-mesosphere-electrodynamics general circulation model, *J. Geophys. Res.*, *106*(A11), 24,869–24,882, doi:10.1029/2001JA000057.

Hagan, M. E., A. Maute, R. G. Roble, A. D. Richmond, T. J. Immel, and S. L. England (2007), Connections between deep tropical clouds and the Earth's ionosphere, *Geophys. Res. Lett.*, *34*, L20109, doi:10.1029/2007GL030142.

Hagan, M. E., A. Maute, and R. G. Roble (2009), Tropospheric tidal effects on the middle and upper atmosphere, *J. Geophys. Res.*, *114*, A01302, doi:10.1029/2008JA013637.

Häusler, K., H. Lühr, M. E. Hagan, A. Maute, and R. G. Roble (2010), Comparison of CHAMP and TIME-GCM nonmigrating tidal signals in the thermospheric zonal wind, *J. Geophys. Res.*, *115*, D00I08, doi:10.1029/2009JD012394.

Heelis, R. A., J. K. Lowell, and R. W. Spiro (1982), A model of the high-latitude ionospheric convection pattern, *J. Geophys. Res.*, *87*(A8), 6339–6345, doi:10.1029/JA087iA08p06339.

Immel, T. J., E. Sagawa, S. L. England, S. B. Henderson, M. E. Hagan, S. B. Mende, H. U. Frey, C. M. Swenson, and L. J. Paxton (2006), Control of equatorial ionospheric morphology by atmospheric tides, *Geophys. Res. Lett.*, *33*, L15108, doi:10.1029/2006GL026161.

Jin, H., Y. Miyoshi, D. Pancheva, P. Mukhtarov, H. Fujiwara, and H. Shinagawa (2012), Response of migrating tides to the stratospheric sudden warming in 2009 and their effects on the ionosphere studied by a whole atmosphere-ionosphere model GAIA with COSMIC and TIMED/SABER observations, *J. Geophys. Res.*, *117*, A10323, doi:10.1029/2012JA017650.

Jones, M., J. M. Forbes, M. E. Hagan, and A. Maute (2013), Non-migrating tides in the ionosphere-thermosphere: In situ versus tropospheric sources, *J. Geophys. Res. Space Physics*, *118*, 2438–2451, doi:10.1002/jgra.50257.

Kil, H., S.-J. Oh, M. C. Kelley, L. J. Paxton, S. L. England, E. Talaat, K.-W. Min, and S.-Y. Su (2007), Longitudinal structure of the vertical $E \times B$ drift and ion density seen from ROCSAT-1, *Geophys. Res. Lett.*, *34*, L14110, doi:10.1029/2007GL030018.

Lin, C., J. Lin, L. Chang, W. Chen, C. Chen, and J. Liu (2013), Stratospheric sudden warming effects on the ionospheric migrating tides during 2008–2010 observed by FORMOSAT-3/COSMIC, *J. Atmos. Sol. Terr. Phys.*, *103*, 66–75, doi:10.1016/j.jastp.2013.03.026.

Lin, C. H., C. C. Hsiao, J. Y. Liu, and C. H. Liu (2007), Longitudinal structure of the equatorial ionosphere: Time evolution of the four-peaked EIA structure, *J. Geophys. Res.*, *112*, A12305, doi:10.1029/2007JA012455.

Liu, H., H. Jin, Y. Miyoshi, H. Fujiwara, and H. Shinagawa (2013a), Upper atmosphere response to stratosphere sudden warming: Local time and height dependence simulated by GAIA model, *Geophys. Res. Lett.*, *40*, 635–640, doi:10.1002/grl.50146.

Liu, H.-L., and R. G. Roble (2002), A study of a self-generated stratospheric sudden warming and its mesospheric-lower thermospheric impacts using the coupled TIME-GCM/CCM3, *J. Geophys. Res.*, *107*(D23), 4695, doi:10.1029/2001JD001533.

Liu, H.-L., V. Yudin, and R. G. Roble (2013b), Day-to-day ionospheric variability due to lower atmosphere perturbations, *Geophys. Res. Lett.*, *40*, 665–670, doi:10.1002/grl.50125.

Manney, G. L., et al. (2008), The evolution of the stratopause during the 2006 major warming: Satellite data and assimilated meteorological analyses, *J. Geophys. Res.*, *113*, D11115, doi:10.1029/2007JD009097.

Matsuno, T. (1971), A dynamical model of the stratospheric sudden warming, *J. Atmos. Sci.*, *28*(8), 1479–1494.

Maute, A., A. D. Richmond, and R. G. Roble (2012), Sources of low-latitude ionospheric $E \times B$ drifts and their variability, *J. Geophys. Res.*, *117*, A06312, doi:10.1029/2011JA017502.

Oberheide, J., and J. M. Forbes (2008), Tidal propagation of deep tropical cloud signatures into the thermosphere from TIMED observations, *Geophys. Res. Lett.*, *35*, L04816, doi:10.1029/2007GL032397.

Oberheide, J., Q. Wu, T. Killeen, M. Hagan, and R. Roble (2007), A climatology of nonmigrating semidiurnal tides from TIMED Doppler Interferometer (TIDI) wind data, *J. Atmos. Sol. Terr. Phys.*, *69*(17-18), 2203–2218, doi:10.1016/j.jastp.2007.05.010.

Oberheide, J., J. M. Forbes, X. Zhang, and S. L. Bruinsma (2011), Wave-driven variability in the ionosphere-thermosphere-mesosphere system from TIMED observations: What contributes to the "wave 4"?, *J. Geophys. Res.*, *116*, A01306, doi:10.1029/2010JA015911.

Pancheva, D., Y. Miyoshi, P. Mukhtarov, H. Jin, H. Shinagawa, and H. Fujiwara (2012), Global response of the ionosphere to atmospheric tides forced from below: Comparison between COSMIC measurements and simulations by atmosphere-ionosphere coupled model GAIA, *J. Geophys. Res.*, *117*, A07319, doi:10.1029/2011JA017452.

Park, J., H. Lühr, M. Kunze, B. G. Fejer, and K. W. Min (2012), Effect of sudden stratospheric warming on lunar tidal modulation of the equatorial electrojet, *J. Geophys. Res.*, *117*, A03306, doi:10.1029/2011JA017351.

Pedatella, N., and J. M. Forbes (2010), Evidence for stratosphere sudden warming-ionosphere coupling due to vertically propagating tides, *Geophys. Res. Lett.*, *37*, L11104, doi:10.1029/2010GL043560.

Pedatella, N. M., and H. Liu (2013), The influence of atmospheric tide and planetary wave variability during sudden stratosphere warmings on the low latitude ionosphere, *J. Geophys. Res. Space Physics*, *118*, 5333–5347, doi:10.1002/jgra.50492.

Pedatella, N. M., J. M. Forbes, and J. Oberheide (2008), Intra-annual variability of the low-latitude ionosphere due to nonmigrating tides, *Geophys. Res. Lett.*, *35*, L18104, doi:10.1029/2008GL035332.

Pedatella, N., H.-L. Liu, A. D. Richmond, A. Maute, and T.-W. Fang (2012a), Simulations of solar and lunar tidal variability in the mesosphere and lower thermosphere during sudden stratosphere warmings and their influence on the low-latitude ionosphere, *J. Geophys. Res.*, *117*, A08326, doi:10.1029/2012JA017858.

Pedatella, N. M., M. E. Hagan, and A. Maute (2012b), The comparative importance of DE3, SE2, and SPW4 on the generation of wavenumber-4 longitude structures in the low-latitude ionosphere during September equinox, *Geophys. Res. Lett.*, *39*, L19108, doi:10.1029/2012GL053643.

Richmond, A., and A. Maute (2013), Ionospheric electrodynamics modeling, in *Modeling the Ionosphere-Thermosphere, Geophysical Monograph Series*, vol. 201, edited by J. Huba, pp. 360, AGU, Washhington, D. C.

Rishbeth, H. (2006), *F* region links with the lower atmosphere?, *J. Atmos. Sol. Terr. Phys.*, *68*(3-5), 469–478, doi:10.1016/j.jastp.2005.03.017.

Roble, R. (1995), Energetics of the mesosphere and thermosphere, in *The Upper Mesosphere and Lower Thermosphere: A Review of Experiment and Theory, Geophys. Monogr. Ser.*, vol. 87, edited by R. Johnson and T. Killeen, pp. 1–22, AGU, Washhington, D. C.

Roble, R. (1996), The NCAR thermosphere-ionosphere-mesophere-electrodynamics general circulation model (TIME-GCM), in *Solar-Terrestrial Energy Program: Handbook of Ionospheric Models*, edited by R. Schunk, pp. 281–288, Utah State University, Logaan, UT.

Rodrigues, F. S., G. Crowley, S. M. I. Azeem, and R. A. Heelis (2011), C/NOFS observations of the equatorial ionospheric electric field response to the 2009 major sudden stratospheric warming event, *J. Geophys. Res.*, *116*, A09316, doi:10.1029/2011JA016660.

Siskind, D., S. D. Eckermann, J. P. McCormack, L. Coy, K. W. Hoppel, and N. L. Baker (2010), Case studies of the mesospheric response to recent minor, major, and extended stratospheric warmings, *J. Geophys. Res.*, *115*, D00N03, doi:10.1029/2010JD014114.

Smith, A. (2012), Global dynamics of the MLT, *Surv. Geophys.*, *33*, 1177–1230, doi:10.1007/s10712-012-9196-9.

Smith, A., and D. Ortland (2001), Modeling and analysis of the structure and generation of the terdiurnal tide, *J. Atmos. Sci.*, *58*, 3116–3134, doi:10.1175/1520-0469(2001)0583116:MAAOTS2.0.CO;2.

Smith, A., M. López-Puertas, M. Garcia-Comas, and S. Tukiainen (2009), SABER observations of mesospheric ozone during NH late winter 2002–2009, *Geophys. Res. Lett.*, *36*, L23804, doi:10.1029/2009GL040942.

Smith, A. K. (2003), The origin of stationary planetary waves in the upper mesosphere, *J. Atmos. Sci.*, *60*(24), 3033–3041.

Sridharan, S., S. Sathishkumar, and S. Gurubaran (2009), Variabilities of mesospheric tides and equatorial electrojet strength during major stratospheric warming events, *Ann. Geophys.*, *27*(11), 4125–4130, doi:10.5194/angeo-27-4125-2009.

Sripathi, S., and A. Bhattacharyya (2012), Quiet time variability of the GPS TEC and EEJ strength over Indian region associated with major sudden stratospheric warming events during 2005/2006, *J. Geophys. Res.*, *117*, A05305, doi:10.1029/2011JA017103.

Stening, R. J. (1986), Lunar effects in the *F* region of the ionosphere, *J. Geophys. Res.*, *91*(A4), 4581–4584, doi:10.1029/JA091iA04p04581.

Stening, R. J., and B. G. Fejer (2001), Lunar tide in the equatorial *F* region vertical ion drift velocity, *J. Geophys. Res.*, *106*(A1), 221–226, doi:10.1029/2000JA000175.

Talaat, E., and R. S. Lieberman (2010), Direct observations of nonmigrating diurnal tides in the equatorial thermosphere, *Geophys. Res. Lett.*, *37*, L04803, doi:10.1029/2009GL041845.

Wang, H., T. J. Fuller-Rowell, R. A. Akmaev, M. Hu, D. T. Kleist, and M. D. Iredell (2011), First simulations with a whole atmosphere data assimilation and forecast system: The January 2009 major sudden stratospheric warming, *J. Geophys. Res.*, *116*, A12321, doi:10.1029/2011JA017081.

Yue, X., W. S. Schreiner, J. Lei, C. Rocken, D. C. Hunt, Y.-H. Kuo, and W. Wan (2010), Global ionospheric response observed by COSMIC satellites during the January 2009 stratospheric sudden warming event, *J. Geophys. Res.*, *115*, A00G09, doi:10.1029/2010JA015466.